PHYSICAL REVIEW B **92**, 020506(R) (2015)

Superconductivity by Sr intercalation in the layered topological insulator Bi_2Se_3

Shruti, V. K. Maurya, P. Neha, P. Srivastava, and S. Patnaik*
School of Physical Sciences, Jawaharlal Nehru University, New Delhi 110067, India
(Received 20 May 2015; revised manuscript received 18 June 2015; published 15 July 2015)

Strontium intercalation between van der Waals bonded layers of the topological insulator Bi_2Se_3 is found to induce superconductivity with a maximum T_c of 2.9 K. Transport measurement on a single crystal of the optimally doped sample $Sr_{0.1}Bi_2Se_3$ shows weak anisotropy ($\Gamma \sim 1.5$) and an upper critical field $H_{c2}(0)$ equal to 2.1 T for a magnetic field applied perpendicular to the c axis of the sample. The Ginzburg-Landau coherence lengths are found to be $\xi_{ab} = 15.3$ nm and $\xi_c = 10.2$ nm. The lower critical field $H_{c1,ab}(0)$ and zero temperature penetration depth $\lambda_{ab}(0)$ are estimated to be 0.39 ± 0.02 mT and 1221 ± 36 nm, respectively. Hall and Seebeck measurements confirm the dominance of electronic conduction, and the carrier concentration is surprisingly low ($n = 1.85 \times 10^{19}$ cm^{-3}) at 10 K, indicating the possibility of unconventional superconductivity.

DOI: 10.1103/PhysRevB.92.020506 PACS number(s): 74.70.−b, 74.25.−q, 74.10.+v, 74.90.+n

I. INTRODUCTION

Superconductors derived from topological insulating phases of quantum matter are among the most profound developments of the recent past [1–3]. Extensively studied three-dimensional topological insulators (TIs), such as Bi_2Se_3 and SnTe, are characterized by gapless spin polarized surface states that emerge from the peculiar topology of an insulating bulk band structure [4]. These surface states show a Dirac-like linear dispersion with the spin polarization locked perpendicular to the electron momentum [5]. Correspondingly, theoretical predictions on a superconducting analog, a fully gapped odd parity pairing state with gapless Majorana surface states, have attracted significant attention [4]. In this Rapid Communication we describe the synthesis and extensive electromagnetic characterization of one such possible example: superconductivity in Sr-intercalated Bi_2Se_3.

Pristine Bi_2Se_3 is a wide band semiconductor with a layered crystal structure. It is made from double layers of $BiSe_6$ octahedra ($R\bar{3}m$, space group 166) consisting of stacked Se-Bi-Se-Bi-Se quintuple layers. These are weakly van der Waals bonded to the neighboring set of layers [6]. As seen in other chalcogenides [7], this layered structure leads to intercalative chemical maneuverings, and topological superconductivity ($T_c \sim 3.5$ K) has been reported in Cu-intercalated Bi_2Se_3 ($Cu_xBi_2Se_3$, $0.12 < x < 0.15$) [1,2]. Further, at high pressure, Bi_2Te_3, Bi_2Se_3, and Sb_2Te_3 are reported to be superconducting [8–10]. A recent study on In-doped SnTe has also shown superconductivity with a T_c of ∼4.5 K [11,12]. Very recently, intercalation of Sr in Bi_2Se_3 was reported with $T_c \sim 2.5$ K, with a large shielding fraction of 88% [13]. In this Rapid Communication we report a successful synthesis of single crystals of Sr-intercalated $Sr_xBi_2Se_3$ with an optimal T_c of 2.9 K for $x = 0.1$.

II. EXPERIMENT

Single crystals of $Sr_xBi_2Se_3$ for $x = 0$, 0.05, 0.1, 0.15, 0.20 were prepared by melting stoichiometric amounts of high purity elements of Bi (99.999%), Se (99.999%), and Sr (99%) at 850 °C in sealed evacuated quartz tubes for 8 days, followed by slow cooling to 650 °C at a rate of 10 °C/h. The sample was then quenched in ice water. The obtained crystals were silvery and shiny with a mirrorlike surface and were easily cleaved along the basal plane of the crystal. The samples remained silvery and shiny even after exposure to air for a long time, unlike $Cu_xBi_2Se_3$, where the sample surface turned golden brown after 1 day exposure to air [2]. The dimensions of the cleaved $Sr_xBi_2Se_3$ crystals were approximately $3 \times 2 \times 0.5$ mm^3. The samples were characterized by powder x-ray diffraction at room temperature using a Rigaku powder x-ray diffractometer (Miniflex-600 with Cu$K\alpha$ radiation). Energy dispersive x-ray spectroscopy (EDAX) and scanning electron microscopy (SEM) images were obtained from a Bruker AXS microanalyzer and from a Zeiss EVO40 SEM analyzer, respectively. High resolution transmission electron microscopy (HRTEM) measurement was done using a JEOL (JEM-2100F) transmission electron microscope. Resistivity, Hall, and magnetization measurements were carried out using a 14 T *Cryogenics* physical property measurement system (PPMS). The Seebeck coefficient was measured from room temperature down to 50 K using a home-built setup. As discussed below, in transport and magnetization measurements, it was confirmed that $x = 0.1$ is the optimal sample with a large superconducting shielding fraction, and in this Rapid Communication we emphasize on this composition.

III. RESULT AND DISCUSSION

Figure 1(a) shows the x-ray diffraction (XRD) data along the basal plane reflections from $Sr_{0.1}Bi_2Se_3$. The sharp peaks along (00l) confirm single crystalline growth of the sample. All the samples were subjected to EDAX, and the pattern for $Sr_{0.1}Bi_2Se_3$ is shown in inset (i) of Fig. 1(a). A quantitative analysis of the EDAX acquired through several points on the sample surface gave the percentage of the element close to stoichiometric values. For example, for $Sr_{0.1}Bi_2Se_3$, the average atomic percentages of Sr, Bi, and Se are found to be 1%, 38%, and 61%, respectively. All the samples show a characteristic layered morphology, as seen in inset (ii) of Fig. 1(a). The schematic unit cell of $Sr_xBi_2Se_3$ is also included.

XRD data of $Sr_xBi_2Se_3$ samples ($x = 0$, 0.05, 0.1, 0.15 and 0.2) were Rietveld refined by FULLPROF software using

*spatnaik@mail.jnu.ac.in

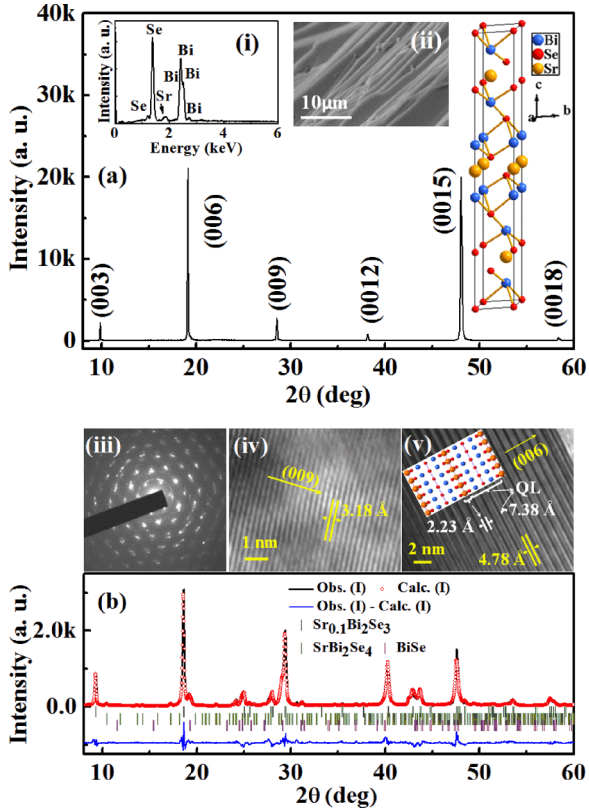

FIG. 1. (Color online) X-ray diffraction data of single crystal $Sr_{0.1}Bi_2Se_3$. Inset (i) shows the EDAX data and inset (ii) shows the SEM image that confirms the layered morphology. The schematic unit cell is also included. The main panel of (b) shows refined XRD patterns for $Sr_{0.1}Bi_2Se_3$. The Bragg position for impurity phases $SrBi_2Se_4$ and BiSe are marked. Inset (iii) shows the diffraction pattern of $Sr_{0.1}Bi_2Se_3$. In inset (iv) the HRTEM images show (009) planes. The HRTEM image of inset (v) shows (006) planes.

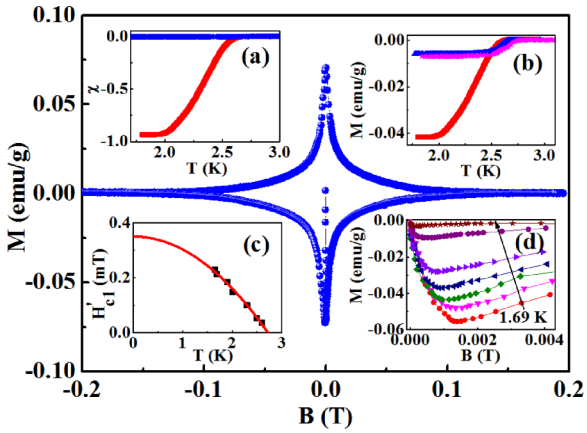

FIG. 2. (Color online) The M-H loop with the $H \parallel ab$ plane at 1.65 K is shown for $Sr_{0.1}Bi_2Se_3$. In inset (a) the dc susceptibilities measured with the $H \parallel ab$ plane under ZFC (red) and FC (blue) conditions are plotted for the 5 G field. Inset (b) shows the dc magnetization graphs under ZFC for $x = 0.1$, 0.15, and 0.2 Sr-intercalated Bi_2Se_3 samples. Inset (c) shows the lower critical field H_{c1} data points (black) and the parabolic fitting (red) line. Inset (d) shows the M-H scan in the low field range at $T = 1.69$, 1.9, 1.97, 2.0, 2.3, 2.5, and 2.6 K.

reported Wyckoff positions [14]. The main panel of Fig. 1(b) shows the refined XRD patterns of $Sr_{0.1}Bi_2Se_3$. The Bi_2Se_3 system crystallizes in a rhombohedral structure with the space group $R\bar{3}m$. It is understood that the Sr atom in the van der Waals gap goes to octahedrally coordinated $3b$ (0,0,1/2) sites [2,7]. Two impurity phases, BiSe and $SrBi_2Se_4$, are also present in the samples, and their concentration grows with an increase in Sr percentage. These impurity phases have been taken into account for better refinement. The percentage compositions of each phase in the optimally doped sample with $x = 0.1$ are $Sr_{0.1}Bi_2Se_3 = 90.97\%$, BiSe = 7.05%, and $SrBi_2Se_4 = 1.98\%$. The refined lattice constants of Bi_2Se_3, $a = 4.14$ Å and $c = 28.64$ Å, are in agreement with reported data [13,15]. Evidently, the c axis increases after Sr intercalation with $a = 4.14$ Å and $c = 28.65$ Å for $Sr_{0.1}Bi_2Se_3$ [13]. The overall volume of the unit cell was found to increase from 425.22 to 425.38, 425.40, 426.20, and 426.55 Å^3 for $x = 0.0$, 0.05, 0.1, 0.15, and 0.2, respectively. This confirms successful intercalation of Sr into Bi_2Se_3 for $0.05 < x < 0.2$.

The superlattice pattern in the electron diffraction measurements is a strong indicator of intercalation [16]. Inset (iii) in Fig. 1(b) shows the diffraction pattern for $Sr_{0.1}Bi_2Se_3$, which demonstrates a diffused, azimuthal spread of the superlattice satellite spots associated with each Bi_2Se_3 Bragg spot. The diffuse nature of the spots suggests a lower intercalant concentration, and the azimuthal spread is due to the large atomic radii of Sr [16]. Insets (iv) and (v) show the HRTEM images for $Sr_{0.1}Bi_2Se_3$ along the (009) and (006) planes, respectively. The HRTEM shows no sign of stacking faults, intergrowths, or amorphous regions. The d values measured from the fringes for $Sr_{0.1}Bi_2Se_3$ corresponding to the (009) and (006) planes are 3.18 and 4.78 Å, respectively. In inset (v) the width of the dark lines corresponds to the distance between the quintuple layers. Moreover, there is a small and broad gap between the fringes that appears alternatively. The broader gap corresponds to the spacing between two quintuple layers (QLs), as shown in schematic for the (006) plane [Fig. 1(b)(v)]. The measured spacing of 2.23 Å from the HRTEM image corroborates well with the XRD result.

The dc magnetization measured for $Sr_{0.1}Bi_2Se_3$ with $H \parallel ab$ under zero field cooled (ZFC) and field cooled (FC) protocols using a 5 G magnetic field is shown in inset (a) of Fig. 2. The onset of the diamagnetic signal is marked at 2.67 K. The superconducting shielding fraction is about 93%, as measured from ZFC data. The magnetization data taken in the FC measurement do not show significant flux trapping, implying the absence of effective pinning centers in the single crystals. Inset (b) of Fig. 2 shows the same measurement for the $x = 0.1$, 0.15, and 0.2 $Sr_xBi_2Se_3$ samples. All the samples within the composition range $0.1 < x < 0.2$ showed superconductivity with a maximum of 2.75 K for $x = 0.2$, but the superconducting shielding fraction decreased with an increase in the Sr concentration. The M-H loop with $H \parallel ab$ at 1.65 K shown in the main panel of Fig. 2 reflects type-II superconductivity with an identifiable irreversibility and upper critical fields. Inset (d) in Fig. 2 shows the M-H scan in a smaller field range at different temperatures towards measuring the lower critical field, which is marked by a deviation from

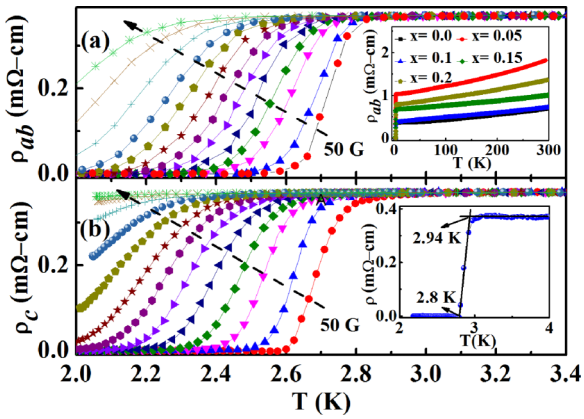

FIG. 3. (Color online) The resistivity as a function of magnetic field applied (a) parallel to the ab plane and (b) parallel to the c axis is plotted for $Sr_{0.1}Bi_2Se_3$. External field $H = 0.005$, 0.02, 0.05, 0.08, 0.11, 0.14, 0.17, 0.20, 0.24, 0.28, 0.34, 0.42, and 0.50 T. The inset in (a) shows the resistivity behavior from 2 to 300 K. The inset in (b) shows the expanded view of the superconducting transition.

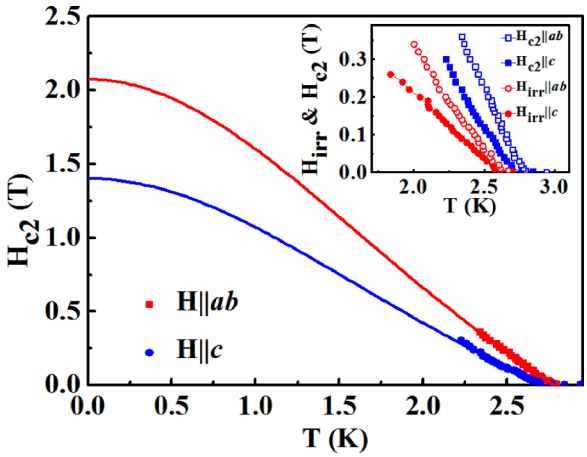

FIG. 4. (Color online) The extrapolated Ginzburg-Landau upper critical field (H_{c2}) as a function of temperature for superconducting $Sr_{0.1}Bi_2Se_3$. The inset shows the upper critical field $H_{c2}(T)$ and $H_{irr}(T)$ found from the onset and offset temperatures for magnetic fields applied parallel and perpendicular to the c axis.

linearity in the diamagnetic state. Using this criterion, a set of $H'_{c1}(T)$ with $H \parallel ab$ was estimated and fitted to the parabolic T dependence $H'_{c1}(T) = H'_{c1}(0)[1-(T/T_c)^2]$, and the experimental lower critical field $H'_{c1,ab}(0)$ is estimated to be 0.35 ± 0.01 mT. This is shown in inset (c) of Fig. 2. Although the demagnetization effect is small for $H \parallel ab$, the corrected value of the lower critical field H_{c1} after demagnetization correction was calculated from $H'_{c1}(0)$ by using Brandt's formula $H_{c1}(0) = H'_{c1}(0)/\tanh\sqrt{0.36b/a}$ for approximate slab geometry [17]. For the aspect ratio $b/a = 3/0.5$, $H_{c1\parallel ab}(0)$ comes out to be 0.39 ± 0.02 mT, which is used for further quantitative analysis.

In Fig. 3 we summarize the magnetotransport measurements. The inset in Fig. 3(a) shows the resistivity from low temperature to room temperature of $Sr_xBi_2Se_3$. For $Sr_{0.1}Bi_2Se_3$, we find a $T_{c\text{-onset}} = 2.94$ K and $T_{c\text{-zero}} = 2.8$ K. This is higher by ~0.35 K as compared to a previous report [13]. A further increase in Sr concentration does not significantly affect the resistive T_c, but the impurity concentration goes up. The resistivity of $Sr_{0.1}Bi_2Se_3$ is linear in the entire temperature range with a residual resistivity $\rho_0 = 0.368 \times 10^{-5}$ Ω m. A sharp superconducting transition with a transition width $\Delta T_c = T_{c\text{-onset}} - T_{c\text{-zero}} = 0.16$ K [inset of Fig. 3(b)] and residual resistivity ratio ($\rho_{300\text{ K}}/\rho_{3\text{ K}} = 1.95$) are observed. As shown in the main panel of Fig. 3, with the application of an external magnetic field, a larger shift in the superconducting transition is observed for the $H \parallel c$ axis than for the $H \parallel ab$ plane. This behavior is reflective of anisotropic transport in layered superconductors, as evidenced in $Cu_xBi_2Se_3$ as well [2].

From the onset and offset data of the superconducting transition in the presence of magnetic fields (Fig. 3), in the inset of Fig. 4 we plot the upper critical field (H_{c2}) and the irreversibility field (H_{irr}) as a function of temperature. The standard criterion used for these estimations is described elsewhere [18]. Further, in a weak coupling case, the Pauli limited upper critical field is given by $H_P(0) = 1.84T_c = 5.15$ T. Under the generalized Ginzburg-Landau model, $H_{c2}(T) = H_{c2}(0)[(1-t^2)/(1+t^2)]$, where $t = T/T_c$. In the main panel of Fig. 4, fitting of our data to this equation gives $H_{c2} \parallel ab(0) = 2.1 \pm 0.025$ T (red line) and $H_{c2} \parallel c(0) = 1.4 \pm 0.035$ T (blue line). In conventional single band Werthamer-Helfand-Hohenberg (WHH) theory, [19] the orbital limited upper critical field of the type- II superconductor in the clean limit is described by $H_{c2} = -0.72T_c(dH_{c2}/dT)_{T_c}$ and is estimated to be 1.6 T for $H \parallel ab$. Since $H_{c2}^{\text{orb}}(0) < H_{c2}(0) < H_P(0)$, the superconductivity in $Sr_{0.1}Bi_2Se_3$ is Pauli limited. With a Maki parameter $\alpha = \sqrt{2}H_{c2}^{\text{orb}}(0)/H_P(0)$ of less than 1, the Flude-Ferrell-Larkin-Ovchinnikov (FFLO) state, which is reflective of the spatially modulated order parameter, is not indicated [20]. The electronic anisotropy parameter $\Gamma \equiv H_{c2,ab}/H_{c2,c} = \lambda_c/\lambda_{ab}$ is about 1.5, and using the anisotropic Ginzburg-Landau formulas [21] $H_{c2,ab} = \phi_0/(2\pi\xi_{ab}\xi_c)$ and $H_{c2,c} = \phi_0/(2\pi\xi_{ab}^2)$, with $\phi_0 = 2.07 \times 10^{-7}$ G cm^2, the Ginzburg-Landau (GL) coherence lengths are estimated as $\xi_{ab} = 15.3 \pm 0.1$ nm and $\xi_c = 10.2 \pm 0.1$ nm. The GL parameters along the two field directions are defined as $\kappa_{ab} = \sqrt{\lambda_{ab}\lambda_c}/\xi_{ab}\xi_c$ and $\kappa_c = \lambda_{ab}/\xi_{ab}$ [22–24]. Using $H_{c1,ab} = (\phi_0/4\pi\lambda_{ab}\lambda_c)(\ln\kappa_{ab} + 0.5)$ [25] and GL formulas, $H_{c2,ab}/H_{c1,ab} = 2\kappa_{ab}^2/(\ln\kappa_{ab} + 0.5)$ gives $\kappa_{ab} = 119.2 \pm 2.6$. Further, from the $H_{c1,ab}$ formula and $\lambda_c = \Gamma\lambda_{ab}$ we get $\lambda_{ab}(0) = 1221 \pm 36$ nm.

To shed more light on the normal state transport properties of the compound, in Fig. 5 we present Hall and thermoelectric power data on a single crystal of $Sr_{0.1}Bi_2Se_3$. As shown in inset (a) of Fig. 5, the Seebeck coefficient S remains negative at all temperatures, indicating electronic charge transport. Inset (b) of Fig. 5 shows the magnetic field dependence of transverse resistivity at 10 K. The ρ_{xy} shows a linear behavior with magnetic field and is negative. The main panel of Fig. 5 shows the Hall coefficient R_H as a function of temperature. R_H is found to be increasing monotonically with temperature up to 200 K. From R_H ($=-1/ne$) the charge carrier density n has been plotted with respect to temperature in inset (c) of Fig. 5. The value of $n = 1.85 \times 10^{19}$ cm^{-3} at 10 K is one order of magnitude less than the Cu-intercalated Bi_2Se_3 [2]. It is indeed

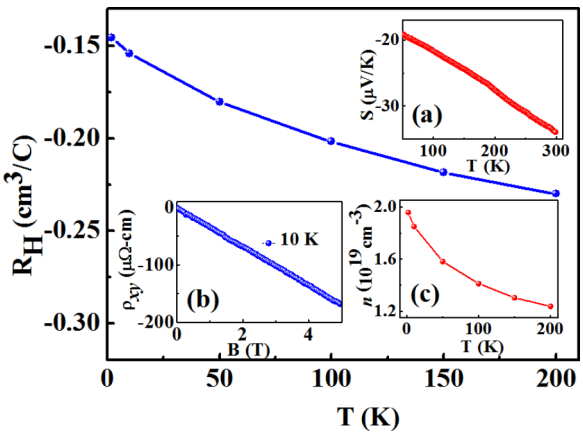

FIG. 5. (Color online) Plot of the Hall coefficient R_H as a function of temperature measured on a single crystal of $Sr_{0.1}Bi_2Se_3$. Inset (a) shows the temperature dependence of the Seebeck coefficient (S). Inset (b) shows the magnetic field dependence of transverse resistivity at 10 K. Charge carrier density n is plotted as a function of temperature in inset (c).

surprising to see superconductivity at 2.9 K with such a low carrier concentration, and most likely a non-BCS mechanism is at play, as is the case in $Cu_xBi_2Se_3$ [26]. The normal state magnetoresistance (not shown) was found to be nonlinear for fields up to 12 T.

The low temperature Hall measurement in combination with temperature-dependent thermoelectric power (TEP) data can be used to estimate the effective mass of carriers m^* and the Sommerfeld constant γ [18]. Using a simplistic free electron model and with an electron carrier concentration $n = 1.58 \times 10^{25}$ m^{-3} at 50 K, the Fermi energy (temperature) comes out to be 23 meV (266.8 K). In low carrier concentration metals, the Seebeck coefficient is given by the Mott expression $S = \pi^2 k_B T/(2eT_F)$, where T_F is the Fermi temperature [27,28]. Using $T_F = 266.8$ K in this expression yields a Seebeck coefficient of $-80\ \mu$V K^{-1} at 50 K, which is larger than the measured value of $-19\ \mu$V K^{-1}. This implies an effective mass of electron $m^* = 0.24m_e$ and a corresponding value of the Sommerfeld constant γ equal to 4.0 J/m^3 K^2. The value of m^* is 1.85 times higher than its value in the parent Bi_2Se_3, as calculated from angle-resolved photoemission spectroscopy (ARPES) and Shubnikov–de Haas (SdH) measurements [29,30]. We note that the mean free path for charge carriers is given by the relation $l = hk_F/2\pi\rho_0 ne^2$ [2,26]. Taking $\rho_0 = 0.368 \times 10^{-5}\ \Omega$ m and $n = 1.85 \times 10^{25}$ m^{-3} at 10 K, and assuming a spherical Fermi surface with a wave vector $k_F = (3\pi^2 n)^{1/3} = 8.2 \times 10^8$ m^{-1}, the mean free path l is estimated to be 49.4 nm, which is greater than ξ_{ab} and ξ_c. This confirms that our sample is in the clean limit.

IV. CONCLUSION

In summary, we report superconductivity in the Sr-intercalated topological insulator Bi_2Se_3 with a Sr concentration in the range $0.1 < x < 0.2$. This is achieved at a surprisingly low carrier concentration of 1.85×10^{19} cm^{-3}. An about 93% superconducting shielding fraction is obtained for $x = 0.1$ with onset resistive $T_c = 2.94$ K. The anisotropy in the upper critical field of $Sr_{0.1}Bi_2Se_3$ yields $\Gamma = 1.5$ with an upper critical field $H_{c2}(0)$ equal to 2.1 T for a magnetic field applied parallel to the ab plane of the sample. Corresponding Ginzburg-Landau coherence lengths are $\xi_{ab} = 15.3$ nm and $\xi_c = 10.2$ nm. The lower critical field $H_{c1,ab}(0)$ and zero temperature penetration depth $\lambda_{ab}(0)$ are 0.39 ± 0.02 mT and 1221 ± 36 nm, respectively. Signatures of an unconventional pairing state are indicated.

ACKNOWLEDGMENTS

Shruti, V.K.M., and P.N. acknowledge UGC for support from fellowships. P.S. acknowledges UGC for support from a D. S. Kothari Fellowship. S.P. thanks the FIST program of the Department of Science and Technology, Government of India for low temperature high magnetic field facilities at JNU. Technical support from Advanced Instrumentation Research Facility (JNU) is acknowledged.

[1] L. A. Wray, S. Y. Xu, Y. Xia, Y. S. Hor, D. Qian, A. V. Fe-dorov, A. Bansil, R. J. Cava, and M. Z. Hasan, Nat. Phys. **6**, 855 (2010).

[2] Y. S. Hor, A. J. Williams, J. G. Checkelsky, P. Roushan, J. Seo, Q. Xu, H. W. Zandbergen, A. Yazdani, N. P. Ong, and R. J. Cava, Phys. Rev. Lett. **104**, 057001 (2010).

[3] T. Sato, Y. Tanaka, K. Nakayama, S. Souma, T. Takahashi, S. Sasaki, Z. Ren, A. A. Taskin, K. Segawa, and Y. Ando, Phys. Rev. Lett. **110**, 206804 (2013).

[4] Y. Ando and L. Fu, Annu. Rev. Condens. Matter Phys. **6**, 361 (2015).

[5] M. Neupane, S.-Y. Xu, L. A. Wray, A. Petersen, R. Shankar, N. Alidoust, C. Liu, A. Fedorov, H. Ji, J. M. Allred, Y. S. Hor, T.-R. Chang, H.-T. Jeng, H. Lin, A. Bansil, R. J. Cava, and M. Z. Hasan, Phys. Rev. B **85**, 235406 (2012).

[6] H. Peng, K. Lai, K. Deheng, S. Meister, Y. Chen, X. L. Qi, S. C. Zhang, Z. X. Shen, and Y. Cui, Nat. Mater. **9**, 225 (2010).

[7] E. Moroson, H. W. Zandbergenz, B. S. Dennis, J. W. G. Bos, Y.Onose, T. Klimczuk, A. P. Ramirez, N. P. Ong, and R. J. Cava, Nat. Phys. **2**, 544 (2006).

[8] J. L. Zhang, S. J. Zhang, H. M. Weng, W. Zhang, L. X. Yang, Q. Q. Liu, S. M. Feng, X. C. Wang, R. C. Yu, L. Z. Cao, L. Wang, W. G. Yang, H. Z. Liu, W. Y. Zhao, S. C. Zhang, X. Dai, Z. Fang, and C. Q. Jin, Proc. Natl. Acad. Sci. USA **108**, 24 (2011).

[9] K. Kirshenbaum, P. S. Syers, A. P. Hope, N. P. Butch, J. R. Jeffries, S. T. Weir, J. J. Hamlin, M. B. Maple, Y. K. Vohra, and J. Paglione, Phys. Rev. Lett. **111**, 087001 (2013).

[10] J. Zhu, J. L. Zhang, P. P. Kong, S. J. Zhang, X. H. Yu, J. L. Zhu, Q. Q. Liu, X. Li, R. C. Yu, R. Ahuja, W. G. Yang, G. Y. Shen, H. K. Mao, H. M. Weng, X. Dai, Z. Fang, Y. S. Zhao, and C. Q. Jin, Sci. Rep. **3**, 2016 (2013).

[11] R. D. Zhong, J. A. Schneeloch, X. Y. Shi, Z. J. Xu, C. Zhang, J. M. Tranquada, Q. Li, and G. D. Gu, Phys. Rev. B **88**, 020505(R) (2013).

[12] V. K. Maurya, Shruti, P. Srivastava, and S. Patnaik, Europhys. Lett. **108**, 37010 (2014).

[13] Z. Liu, X. Yao, J. Shao, M. Zuo, L. Pi, S. Tan, C. Zhang, and Y. Zhang, arXiv:1502.01105.

[14] L. Bindi and C. Cipriani, Can. Mineral. **42**, 835 (2004).
[15] G. V. S. Rao and M. W. Shafer, in *Intercalated Layered Materials: Physics and Chemistry of Materials with Layered Structures*, edited by F. A. Lévy (Reidel, Dordrecht, 1979), Vol. 6, p. 99.
[16] K. J. Koski, C. D. Wessells, B. W. Reed, J. J. Cha, D. Kong, and Y. Cui, J. Am. Chem. Soc. **134**, 13773 (2012).
[17] E. H. Brandt, Phys. Rev. B **60**, 11939 (1999).
[18] P. Srivastava, Shruti, and S. Patnaik, Supercond. Sci. Technol. **27**, 055001 (2014).
[19] N. R. Werthamer, E. Helfand, and P. C. Hohenberg, Phys. Rev. **147**, 295 (1966).
[20] F. F. Tafti, T. Fujii, A. Juneau-Fecteau, S. René de Cotret, N. Doiron-Leyraud, A. Asamitsu, and L. Taillefer, Phys. Rev. B **87**, 184504 (2013).
[21] M. Kończykowski, C. J. van der Beek, M. A. Tanatar, V. Mosser, Y. J. Song, Y. S. Kwon, and R. Prozorov, Phys. Rev. B **84**, 180514(R) (2011).
[22] R. A. Klemm, J. Low Temp. Phys. **39**, 589 (1980).
[23] V. G. Kogan, Phys. Rev. B **24**, 1572 (1981).
[24] J. R. Clem, Physica C **162–164**, 1137 (1989).
[25] C.-R. Hu, Phys. Rev. B **6**, 1756 (1972).
[26] T. V. Bay, T. Naka, Y. K. Huang, H. Luigjes, M. S. Golden, and A. de Visser, Phys. Rev. Lett. **108**, 057001 (2012).
[27] C. Kittel, *Introduction to Solid State Physics* (Wiley, New York, 1986).
[28] A. S. Sefat, M. A. McGuire, B. C. Sales, R. Jin, J. Y. Howe, and D. Mandrus, Phys. Rev. B **77**, 174503 (2008).
[29] H. Kholer, Phys. Status Solidi B **58**, 91 (1973).
[30] J. G. Analytis, J.-H. Chu, Y. Chen, F. Corredor, R. D. McDonald, Z. X. Shen, and I. R. Fisher, Phys. Rev. B **81**, 205407 (2010).